

# Single-Walled Carbon Nanotube Purification, Pelletization, and Surfactant-Assisted Dispersion: A Combined TEM and Resonant Micro-Raman Spectroscopy Study

Kai Shen,<sup>†</sup> Seamus Curran,<sup>‡</sup> Huifang Xu,<sup>§</sup> Snezna Rogelj,<sup>||</sup> Yingbing Jiang,<sup>⊥</sup>  
James Dewald,<sup>‡</sup> and Tanja Pietrass<sup>\*,†</sup>

Department of Chemistry, New Mexico Tech, Socorro, New Mexico 87801, Department of Physics, New Mexico State University, Las Cruces, New Mexico 88003, Department of Geology and Geophysics, University of Wisconsin, Madison, Wisconsin 53706, Department of Biology, New Mexico Tech, Socorro, New Mexico 87801, and Transmission Electron Microscopy Laboratory, Department of Earth and Planetary Sciences, University of New Mexico, Albuquerque, New Mexico 87131

Received: October 29, 2004; In Final Form: January 11, 2005

Resonant Raman spectroscopy and transmission electron microscopy were used to characterize the structural changes of three single-walled carbon nanotube samples processed with purification, pelletization, and surfactant-assisted dispersion. A two-stage purification process selectively removes metallic tubes as well as small-diameter ones, enriching large-diameter semiconducting tubes. Pelletizing reduces the intertube distance but greatly increases the intensity ratio of the D band to the G band. Single-walled nanotube (SWNT) bundle size decreases during ultrasonication dispersion aided by a surfactant. SWNT bundles composed of large-diameter tubes are prone to debundling.

## I. Introduction

Carbon nanotubes (CNTs) have been attracting great attention for their possible usages ranging from fabrication of nanoelectronics to fuel tanks because of their unique quasi-one-dimensional structures.<sup>1</sup> Applications in composites and hydrogen storage, especially using single-walled carbon nanotubes (SWNTs), has spurred significant research activity.<sup>2–4</sup> Those studies are impeded mainly because of the complex nature of the samples: SWNTs contain both carbonaceous impurities and metallic catalysts; in addition, SWNTs can be either metallic or semiconducting with a range of diameters and chiralities.<sup>5</sup> The situation becomes worse when considering the multitude of synthesis and processing techniques. To relate structural features to their applications, a detailed study of structural changes after processing is required. We characterize these changes after several processing techniques by studying tube morphology as well as electronic structure. We used commercially available samples synthesized by the most common production methods: carbon arc discharge (CAD) and high-pressure injection of CO (HiPco).

SWNTs can be regarded as rolled-up individual graphene sheets. Theoretical calculations<sup>6</sup> and experimental work<sup>7</sup> confirm the existence of van Hove singularities in the 1D electronic density of states. The unique property of resonance Raman spectroscopy (RRS) on SWNTs is that the Raman scattering will be greatly enhanced when the gap between the singularities matches with either incident or scattered photon energies. Thus, it should be always borne in mind that, for any given excitation wavelength, only a subset of all SWNTs is detected.<sup>8</sup> As the

probe size is 1–2  $\mu\text{m}$  in our experiment, RRS can sample a large population of SWNT bundles. However, the spectra represent only those certain types of tubes that are resonant with the excitation energy. By varying the excitation energy, different tubes can be selectively excited. In addition, compared with scanning probe microscopy, RRS requires a simpler sample preparation and provides a wealth of information not only on morphology, such as tube diameter, but also on electronic structure for both SWNTs and multiwalled nanotubes (MWNTs).<sup>9–11</sup>

As-produced SWNTs are usually contaminated with carbon species such as carbon nanoparticles, fullerenes, carbon onions, graphite, as well as amorphous carbon. In addition, metal species may be present as particles in SWNT bundles.<sup>3,12</sup> To obtain pure CNTs for future research on their properties and applications, a purification procedure is required to remove carbonaceous and metallic impurities. In this study, samples were subjected to a two-stage purification process.<sup>13</sup> The morphology changes, as well as the electronic structure changes, upon purification were monitored by a combination of RRS and transmission electron microscopy (TEM). The differences in SWNT structural characteristics provide information for tweaking purification process parameters to better fit their application.

For SWNTs to be useful as hydrogen storage media,<sup>3,4,14</sup> it is advantageous to form SWNT pellets to increase the volumetric storage ratio. Pelletizing may lead to possible deformation of tubes or reduced intertube distance, which can be monitored by an analysis of the change in Raman-active modes, especially the radial breathing mode (RBM) and the G band. For practical reasons, we use relatively low pressures ( $\sim 8.8$  MPa) to obtain pellets.<sup>11</sup>

It is well-known that the bundles of SWNTs are held together mainly by intertube van der Waals forces. Although both theoretical calculations and experiments suggest preferred hydrogen adsorption in the interstitial channels of SWNT bundles,<sup>15–17</sup> there is a lack of explicit evidence. Recently,

\* Corresponding author. Email: tanja@nmt.edu.

<sup>†</sup> Department of Chemistry, New Mexico Tech.

<sup>‡</sup> Department of Physics, New Mexico State University.

<sup>§</sup> Department of Geology and Geophysics, University of Wisconsin, Madison.

<sup>||</sup> Department of Biology, New Mexico Tech.

<sup>⊥</sup> Department of Earth and Planetary Sciences, University of New Mexico.

**TABLE 1: SWNT Sample Characterization over Purification and Sonication<sup>a</sup>**

	sample	av bundle size/ nm	std dev/ nm	bundle size range/ nm	max bundle size/ nm	min bundle size/ nm	purification yield/ wt %
MRSW	pristine	17.8	6.9	28.7	38.7	10.2	
	acid <sup>b</sup>	11.8	2.7	13.3	19.4	6.1	70.3
	puri. <sup>c</sup>	14.9	8.5	45.2	50.3	4.9	66.4
CNI	pristine	11.4	6.3	29.5	33.5	3.0	
	acid	10.5	4.0	17.7	19.6	1.9	66.2
	puri.	11.0	5.6	25.1	23.6	1.5	30.9
	sonicated	4.9	2.4	14.9	16.1	1.2	
CLex	pristine	~11.0					
	acid	9.3	3.0	12.1	16.7	4.7	50.7
	puri.	10.6	2.7	11.5	17.9	6.4	38.3

<sup>a</sup> For each sample, 120 bundles were measured. Std dev: standard deviation. Bundle size range: difference between maximum and minimum bundle size. <sup>b</sup> Acid: acid-treated. <sup>c</sup> Puri.: sample subjected to two-stage purification process. Purification yield: yield during each single purification step.

various methods have been reported to successfully split SWNT ropes.<sup>18,19</sup> Among them, surfactant-assisted debundling is attractive for its simplicity.<sup>18</sup> By preparing samples with reduced bundle size, we aim to understand the role of SWNT structural characteristics in the debundling process.

In this work, we combine morphology analysis and RRS to analyze the SWNT structural and/or population changes for various treatment processes related to hydrogen adsorption on SWNTs. The paper is organized as follows: We first describe the sample processing procedures and characterization in great detail to ensure reproducibility by other researchers. In the next section, we discuss SWNT structural changes after a two-stage purification procedure using Raman spectroscopy and TEM. We then present and interpret pressure-induced changes of the Raman-active modes upon the pelletization process. Finally, we focus on the effect of surfactant-aided dispersion monitored by Raman spectroscopy. We conclude with a summary of the results.

## II. Experimental Section

Three commercially available SWNT samples (MRSW, CNI, and CLex) were employed in our experiment. A detailed sample description is available elsewhere.<sup>20</sup> In brief, two samples (MRSW and CLex) were synthesized using the CAD technique, whereas the CNI sample was produced by the HiPco process. Inductively coupled plasma/mass spectrometry analysis reveals that the main catalyst components are Co and Ni for MRSW, Fe for CNI, and Ni and Yt in CLex. The sample characterization is summarized in Table 1.

**2.1. Purification Procedure.** A two-stage oxidative purification procedure was employed.<sup>13</sup> The SWNT sample was refluxed in 3 M nitric acid for 16 h. The mixture was filtered and dried overnight. The sample was then air-oxidized at 883 K for 30 min.

**2.2. Pelletizing Process.** The SWNT sample was put onto the stage of a standard press for FT-IR sample preparation. An ~8.8-MPa pressure was applied to ca. 50 mg of MRSW sample and kept for 5 min. The pellet was carefully removed from the stage for Raman data acquisition.

**2.3. Dispersion with Surfactant.** The dispersion process was adapted from O'Connell et al.<sup>18</sup> A 2-mg pristine CNI sample was first stirred in 200 mL of 1 wt % sodium dodecyl sulfate (SDS) solution for 1 h. The suspension was then subjected to sonication in a cup-horn ultrasonicator (Branson Sonifier 450) for 30 min at a power level of 220 W. To avoid overheating during sonication, the solution was kept in an ice-water bath. The sonicated CNI sample was kept stagnant overnight to precipitate metal particles from shattered ultrasonicator tips.<sup>21</sup>

The supernatant was carefully filtered through a Millipore PTFE membrane filter with a pore diameter of 0.22  $\mu\text{m}$  to remove free SDS and SDS micelles. The filter cake was rinsed with distilled water and air-dried.

**2.4. Raman Experiments.** The Raman spectra were acquired on a Renishaw inVia Raman microscope equipped with different laser excitation wavelengths. Generally, the laser beam was focused on the sample with a 50 $\times$  objective (laser spot size  $\approx$  1–2  $\mu\text{m}$ ) of the Raman microscope. The Raman spectra were collected in a backscattering configuration. An exposure time of 10 s with five accumulations was used to obtain a high S/N ratio. Raman spectra were acquired from three randomly selected spots on the sample. A close examination of three runs demonstrated high reproducibility. The Raman microscope was calibrated using the Raman band of silicon at 520  $\text{cm}^{-1}$ . A 785-nm (1.58-eV) laser excitation line was produced from a Renishaw HPNIR785 diode laser with a peak power of 350 mW. The 514.5-nm (2.41-eV) excitation line was generated by a Laser Physics Ar<sup>+</sup> laser. The sample received 1 mW of power.

**2.5. TEM Characterization.** The SWNT morphology before and after purification and dispersion was studied by TEM (JEOL JEM 2010). The specimens for TEM characterization were prepared by depositing the CNT powders directly onto holey carbon-coated copper grids. For every SWNT sample, the sizes of 120 bundles were measured under high magnification using DigitalMicrograph 3.65. The bundle sizes were then analyzed by the software package SPSS (version 11.5 for Windows).

## III. Purification Process

**3.1. TEM Study of Purification Process.** The morphology characterization after the two-stage purification process is summarized in Table 1. A much larger sampling size (120 measurements) than in previous work<sup>20</sup> was used to ensure higher precision.<sup>22</sup> When compared with our previous results, the average bundle sizes show relatively small differences (~5%) for all three samples, demonstrating high reproducibility of our measurements. It should be noted that the measurement of SWNT bundle length is difficult for entangled bundles. Nevertheless, we observed that the lengths of the entangled bundles were greatly reduced after acid treatment, implying the tubes broke lengthwise. Because of the high content of impurities in the CLex parent material as shown in Figure 1c, only approximate bundle sizes could be obtained.

The morphology of the samples immediately after acid reflux was also studied. For all three samples, the acid treatment seemed to reduce the SWNT bundle size to a different degree; both the average and the maximum bundle size decreased. The bundle range, the difference between maximum and minimum



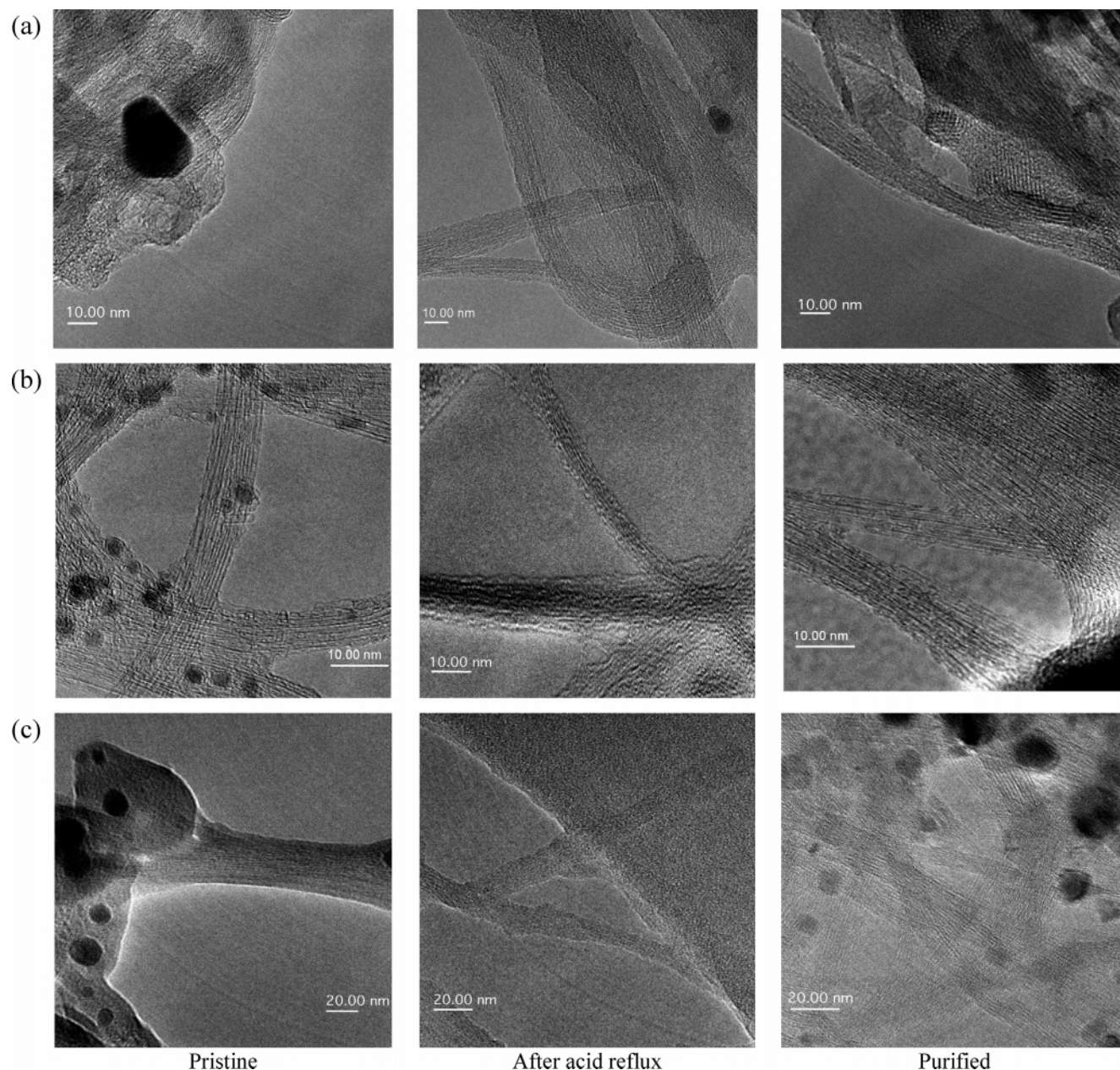


**Figure 1.** TEM micrographs of three SWNT samples subjected to the two-stage purification. Row (a) MRSW; (b) CNI; (c) CLex.

size, also revealed a noticeable decrease. MRSW showed the most evident changes after acid reflux. Because the diameter of MRSW ( $\sim 1.3$  nm) is relatively close to that of CLex ( $\sim 1.4$  nm) and is larger than that of CNI ( $\sim 1$  nm), a possible reason for the more prominent changes in MRSW may be the higher inhomogeneity of tube-diameter distribution in the bundles. Recent results demonstrate that the coupling between individual tubes in bundles is localized,<sup>23</sup> which leads to easier breakage of bundles with a heterogeneous distribution of tube diameters.

As demonstrated previously,<sup>24</sup> oxidative acid reflux introduces functional groups on the tube side walls. The TEM micrographs (Figure 1) show blurred edges of the bundles after acid reflux for all samples, which may be due to the attachment of functional groups to the tube walls. After air oxidation, the edges were restored, implying the removal of those functional groups. When comparing the bundle sizes of all SWNT samples after acid reflux with those after oxidation treatment, it is found that the bundle sizes as well as ranges increase after air oxidation. Air oxidation at 823 K is believed to remove residual amorphous

carbon because of the difference in oxidation temperature for amorphous carbon and SWNTs.<sup>25</sup> The observation of larger bundle sizes after air oxidation can be explained by the selective removal of small bundles, which may be ascribed to their higher specific surface area.

Because of the higher density of the metal impurities, the mass loss during acid reflux is mainly due to the removal of metallic remains in the pristine samples. It is very interesting to examine the yield of the acid-refluxed samples subjected to air oxidation. MRSW shows a much higher (approximately twofold) yield than CNI and CLex despite the fact that MRSW and CLex were both synthesized by CAD. Because air oxidation can only remove carbonaceous materials, the loss of weight can be due to the removal of either amorphous carbon, SWNTs, or both. As shown in Figure 1, the removal of amorphous carbon is fairly complete after acid reflux. The majority of the weight loss during air oxidation for CLex must hence be due to the removal of tubes. The higher resistance to air oxidation of the MRSW sample when compared to CLex may be related to the

**TABLE 2: Raman Spectral Features after a Two-Stage Purification**

		Raman band frequency/cm <sup>-1</sup>									
		RBM		G							
excitation	sample	main	minor	D	shoulder	G <sup>-</sup>	G <sup>+</sup>	G'	I <sub>D</sub> /I <sub>G</sub> <sup>d</sup>		
1.58 eV	MRSW	pristine	310		1295 (29) <sup>c</sup>	1549	1570	1592	2578 (40)	0.034	
		acid <sup>a</sup>			1343 (82)	1555	1572	1596	2590 (47)	0.158	
	CNI	puri. <sup>b</sup>	206	307	1299 (29)	1549	1568	1592	2578 (40)	0.031	
		pristine	233/267		1293 (25)		1563	1594	2578	0.057	
	CLex	acid	241	270	1335 (91)	1544	1571	1603	2612	0.605	
		puri.	206/236		1294 (28)		1565	1594	2572	0.032	
		pristine	306		1292 (53)	1551	1570	1593	2573	0.210	
		acid			1330 (94)		1561	1605	2609	1.029	
	2.41 eV	MRSW	puri.	307		1300 (42)	1551	1570	1592	2575	0.059
			pristine	172		1346 (24)		1573	1584	2683	0.014
CNI		acid									
		puri.	167/176		1344 (19)		1567	1593	2679	0.011	
CLex		pristine	268		1334 (18)	1526	1548	1595	2658	0.041	
		acid									
		puri.	185/205		1338 (21)		1566	1592	2662	0.019	
		pristine	169		1344 (54)		1571	1590	2679	0.050	
		acid									
	puri.	151/167		1348 (18)		1574	1595	2679	0.007		

<sup>a</sup> Acid: acid-treated. <sup>b</sup> Puri.: sample subjected to two-stage purification process. <sup>c</sup> The number in parentheses is the full width at half-maximum (fwhm) of the D band. <sup>d</sup> *I<sub>D</sub>/I<sub>G</sub>*: intensity ratio of D band to the most intense G band (G<sup>+</sup>).

high crystallinity and low defect density of the MRSW tube walls due to the different temperature and/or catalysts used.<sup>26</sup> Because the smaller tubes have higher curvatures and thus higher reactivity,<sup>19</sup> they are oxidized more easily and removed from the sample. The low yield for the CNI sample after air oxidation may be due to its relatively small tube diameter (~1 nm) and possibly low crystallinity caused by its synthesis method (HiPco).<sup>27</sup> Either factor can lead to high reactivity toward oxidation and result in the loss of tubes.

In summary, the acid reflux step can eliminate both metal impurities and amorphous carbon. In addition, the acid treatment can break the SWNT bundle and stabilize small bundles with functional groups attached to the tube wall by oxidative acid attack. The air oxidation removes these groups as well as small diameter tubes. Higher tube crystallinity and large tube size help to preserve the structural integrity of the tubes.

**3.2. Resonance Raman Study of the Two-Stage Purification Process.** The main Raman features are summarized in Table 2. Because of the large amount of functional groups introduced during the acid treatment stage, we focus on the comparison between fully purified and pristine samples. In this study, we used two laser excitation wavelengths in the near-IR (1.58 eV) and visible range (2.41 eV) to probe tube structural and/or tube relative population changes after purification. From a previous study<sup>20</sup> and the TEM analysis outlined already, we concluded that the SWNT bundle size does not change considerably. Thus, the resonant electronic transition change due to bundle size can be neglected in the discussion of the purification process.<sup>28</sup>

**3.2.1. G band.** The G band for SWNTs is an intrinsic Raman-active optical mode and can be observed between 1500 and 1620 cm<sup>-1</sup>, depending on excitation wavelength and nanotube chirality type. For individual SWNTs, the G band typically is composed of two separate peaks. The higher-frequency peak (G<sup>+</sup>) is due to the vibrations along the tube axis, while the lower one (G<sup>-</sup>) is caused by the vibrations along the tube circumference. For semiconducting tubes, both G<sup>+</sup> and G<sup>-</sup> are of Lorentzian shape. Metallic tubes, however, exhibit broad Breit–Wigner–Fano (BWF) line shapes for G<sup>-</sup>, while G<sup>+</sup> has a Lorentzian line shape.<sup>29,30</sup> The G-band transitions before and after purification at the two excitation energies are compiled in Figure 2. The most prominent feature is that there is more than

one G<sup>-</sup> peak in all three samples at 1.58 eV, and also at an excitation energy of 2.41 eV for purified CNI. This may indicate that our SWNT bundles are composed of tubes of different types (diameter and chirality). For SWNT bundles, various types of tubes may lie within “resonant windows”<sup>31</sup> of either incident or scattered photons, leading to the appearance of more than one G<sup>-</sup> peak. At 1.58 eV, MRSW and CLex show the BWF line shape at 1545 cm<sup>-1</sup> and a Lorentzian one around 1565 cm<sup>-1</sup>. A rough estimate of tube diameters can be obtained by using Kataura plots:<sup>32</sup> the metallic tubes have a diameter range of 1.4–1.6 nm, in resonance with E<sub>11</sub><sup>M</sup>, and the semiconducting tubes of 1.2–1.3 nm, in resonance with E<sub>22</sub><sup>S</sup>. The similarity of the spectra and thus the tube structures may be due to their production method (CAD). CNI, produced by HiPco, does not show a remarkable content of metallic tubes at 1.58 eV. At 1.58-eV excitation, both peak frequencies and line widths exhibit negligible changes upon purification. Only MRSW has a lower intensity of the BWF peak, implying the preferred removal of metallic tubes. We will discuss this phenomenon further in combination with changes in the RBM features after purification.

Although the G bands of both MRSW and CLex do not show many changes before and after purification at 2.41-eV excitation, semiconducting tubes are observed for CNI after purification, suggesting the selective removal of metallic tubes. We substituted nitric acid with HCl, a non-oxidative acid, for the two-stage purification. No changes have been observed in the G bands (data not shown here), confirming that nitric acid preferentially eliminates metallic tubes from samples. Strano et al.<sup>33</sup> proposed that metallic tubes have a tendency to stabilize the charge-transfer transition state prior to bond formation. During purification, when oxidative ions such as NO<sub>3</sub><sup>-</sup> attack the SWNT sidewalls, metallic tubes tend to stabilize electron-deficient functional groups such as the carboxyl group. As we only observe partial populations of SWNTs, further Raman experiments with tunable laser energy are required to verify this hypothesis.

**3.2.2. RBM Band.** The low-frequency shift region (50–350 cm<sup>-1</sup>) RBM is of A<sub>1g</sub> symmetry, in which the carbon atoms undergo radial displacement. It has been established that the RBM frequency of individual SWNTs is proportional to the reciprocal of the tube diameter (i.e.,  $\omega_{\text{RBM}} = \alpha/d_t + \Delta\omega_{\text{RBM}}$ ,



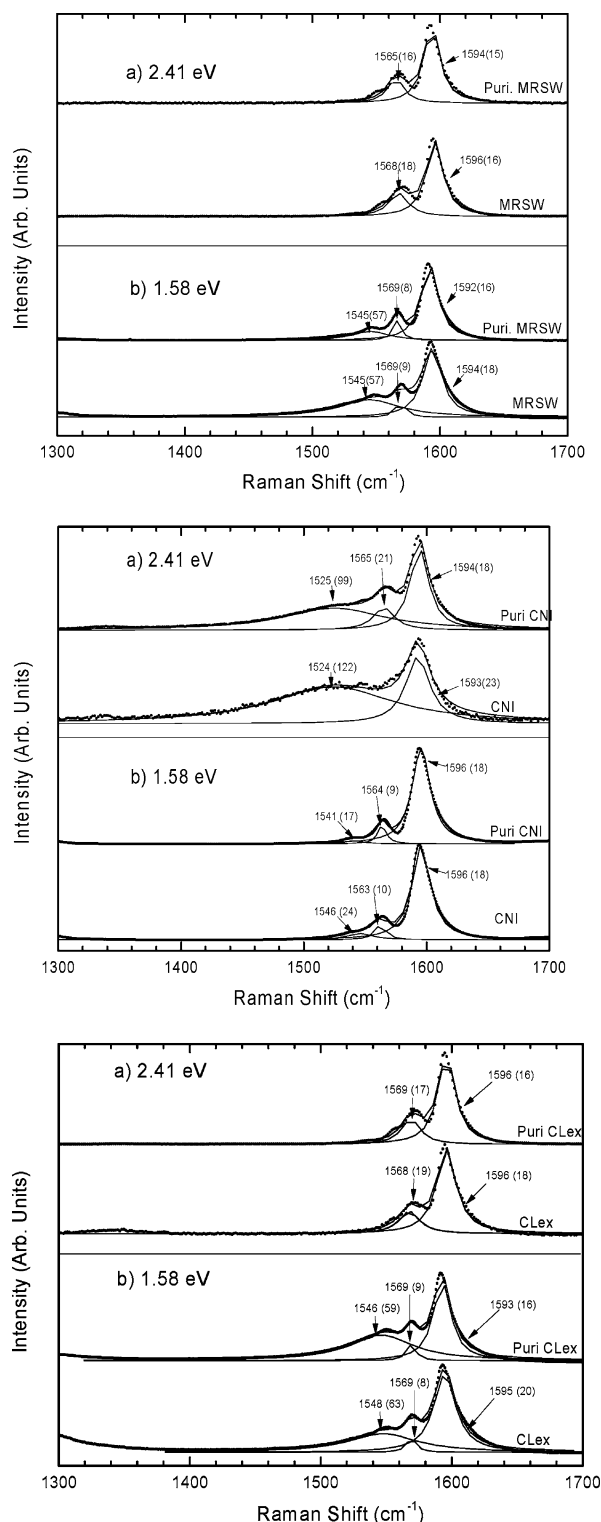


**Figure 2.** Raman spectra of three SWNTs upon purification in the range 1300–1700  $\text{cm}^{-1}$ . Excitation energy is (a) 2.41 eV and (b) 1.58 eV.

where  $\omega_{\text{RBM}}$  is the wavenumber of RBM,  $d_t$  is the SWNT diameter,  $\alpha$  is a proportional factor, and  $\Delta\omega_{\text{RBM}}$  is the offset of RBM wavenumber).<sup>6,11,30,34</sup> Note that the relationship between tube diameter and Raman frequency has been proven only for isolated SWNTs.<sup>35,36</sup> Previous research indicated an  $\sim 10\%$  upshift in the RBM frequencies upon bundling compared to isolated tubes, due to intertube interactions.<sup>37</sup> Because of the localized tube couplings in inhomogeneous bundles<sup>23</sup> as discussed in section 3.1, the upshift in RBM frequencies can only

be ascribed to the change of a resonant electronic transition with bundle size.<sup>28</sup> Despite the controversy over the precise calculation of the diameter through the RBM frequencies, it is safe to use the established relationship mentioned already to study the change of tube type during purification, because all the tubes in our samples have diameters over 0.8 nm.<sup>38</sup> In addition, there is no change of tube type during purification, only the removal of tubes or the functionalization of existing tubes.

Table 2 lists the most prominent RBM bands in the spectra. It should be noted that the Raman spectra from acid-treated samples have very broad line widths and relatively low intensities in the low-frequency range. This may be due to functional groups or defects introduced during oxidative acid reflux.<sup>39</sup> After annealing in stagnant air, the RBM line width (fwhm) decreases and the intensity increases, implying the removal of functional groups and defects. To exclude the interference of those defects, we only compare the pristine samples with those after air oxidation. Several interesting changes can be observed. First, oxidative purification preferentially eliminates small-diameter tubes. For example, at 1.58-eV laser excitation energy, the high-frequency component (310  $\text{cm}^{-1}$ ) of MRSW, produced by the CAD method, disappeared, while a new low-frequency component (206  $\text{cm}^{-1}$ ) emerges. This implies the loss of relatively small diameter tubes (high-frequency component), with only large tubes (low-frequency component) surviving the purification. This coincides with the TEM observation in section 3.1. A similar phenomenon has been observed in our multiwalled carbon nanotube samples.<sup>20</sup> Another interesting observation is that RBM frequencies change upon purification for both excitation wavelengths. Small changes in RBM frequency during purification can be explained by the homogeneity of the tube-diameter distribution in the diameter range excited with a certain photon energy. For samples with fairly uniform diameters, the diameter distribution does not change significantly even with preferential removal of small-diameter tubes. As mentioned already, discrete laser lines excite only limited diameter ranges and certain types of tubes. Here, we assume a “resonant window” of  $\pm 0.1$  eV centered on incoming photon energy.<sup>40,41</sup>

According to Kataura,<sup>32</sup> it is estimated that the 1.58-eV line excites semiconducting tubes within a diameter range 0.9–1.1 nm, and the 2.41-eV line can either be in resonance with 1.2–1.4-nm semiconducting tubes or metallic tubes of 0.9–1.1 nm. Combined with the G-band mode shape at different excitation energies (see section 3.2.1), we can deduce that MRSW has relatively uniform diameter semiconducting tubes but has a large diameter distribution in metallic tubes. From the RBM profiles, it is convenient to monitor the diameter changes over the purification and diameter distribution of different types of SWNTs, which otherwise would be exceedingly difficult to characterize using other microscopy techniques such as TEM or scanning tunneling microscopy.

**3.2.3. D Band and G' Band.** The D band and the G' band are common features in SWNT spectra. The D band is activated by disorders in  $\text{sp}^2$  carbon clusters.<sup>6</sup> The G' band (or D\*) appears at approximately the first overtone of the D band. However, the G' band is an intrinsic feature of the SWNT Raman spectrum, regardless of the disorder present.<sup>40</sup> Both D and G' bands are obtained through a double resonance process<sup>42</sup> in which one of the scattering processes is mediated by a defect. For a certain photon energy excitation (1.58 eV), the D-band frequencies are almost identical for all pristine samples, regardless of their production methods. However, the resonance spectra excited at 2.41 eV reveal differences in D-band frequencies for

SWNTs synthesized from CAD versus HiPco. As discussed in section 3.2.1, the 2.41-eV photons are resonant with metallic tubes for CNI and semiconducting ones for MRSW and CLex. The difference in D-band frequencies may be due to the observation of different types of tubes, hence a different coupling between electrons and phonon density of states during the scattering. Another interesting result is that the D-band frequency upshifts distinctly upon oxidative acid treatment. This shift might be ascribed to the introduction of functional groups and/or loss of carbon atoms from the tube sidewall. For all samples studied, the D-band frequencies return to those of the pristine samples after annealing, suggesting complete removal of those functional groups and vacancies through the rearrangement of carbon atoms on the sidewall. The line width of the D band is related to tube crystallinity and density of defects.<sup>39</sup> The dramatic change of the D-band line width during acid treatment and annealing agrees with the D-band shift during purification. We found, however, that the D-band line width varies significantly ( $\sim 6\text{ cm}^{-1}$ ) at different sampling spots, and caution should be applied when using D-band line widths to monitor the density of defects in SWNT samples.

According to Ferrari et al.,<sup>43</sup> the intensity ratio of G and D bands ( $I_D/I_G$ ) is related to the  $\text{sp}^2$  carbon cluster sizes in the graphene sheet and is nearly proportional to defect density. We calculated the intensity ratio of the D band to that of the most intense G band ( $G^+$ ). Results are listed in Table 2. The  $I_D/I_G$  ratio of pristine CLex is much higher than for the other two samples using 1.58-eV excitation. There are two possible reasons for this exceedingly high ratio. First, the high content of amorphous carbon revealed in the TEM micrographs causes high D-band intensity. Second, the crystallinity of the CLex tubes is lower than that of the other two samples, which may be related to the synthesis conditions such as catalysts and/or temperature. A closer comparison of the intensity ratios of CLex before and after purification showed that the ratio after purification greatly decreased, implying that the large content of amorphous carbon in the pristine sample is responsible for the high  $I_D/I_G$  ratio. TEM micrographs (Figure 1) confirm this hypothesis.

The  $I_D/I_G$  ratio is dispersive. For example, the difference between CLex and the other samples is about a factor of 5 using 1.58-eV excitation, while the difference in the ratios is marginal for 2.41-eV excitation. Because the D peak is due to larger carbon  $\text{sp}^2$  clusters at low excitation energy,<sup>43</sup> the D band at 2.41-eV excitation comes from smaller  $\text{sp}^2$  clusters, whereas at 1.58 eV, it is mainly due to larger-sized amorphous carbon clusters. Consequently, the  $I_D/I_G$  ratio at high excitation can be used to compare the crystallinity of the SWNTs. For example, at 2.41 eV, MRSW demonstrates a much lower intensity ratio when compared with CNI and CLex. It is thus concluded that MRSW has a lower tube-defect density than CNI and CLex.

Because of its disorder origin, the D band is useful in characterizing the defect density in SWNT samples. The addition of functional groups and/or defects into the tube wall causes an upshift of the D-band frequency as well as an increase in the D bandwidth. The  $I_D/I_G$  ratio is a useful tool in monitoring amorphous carbon content at low excitation energy (e.g., 1.58 eV) and comparing the crystallinity of various tubes at high excitation energy (e.g., 2.41 eV).

**3.2.4. Intermediate Frequency Mode.** The intermediate frequency mode (IFM) refers to a Raman-active mode ranging from 600 to 1100  $\text{cm}^{-1}$ . According to group theory, it should be a Raman-silent region for infinitely long tubes.<sup>44</sup> Saito et al.<sup>45</sup> showed that the Raman-active mode in this region may be due to the symmetry-lowering effect from the finite tube size. To

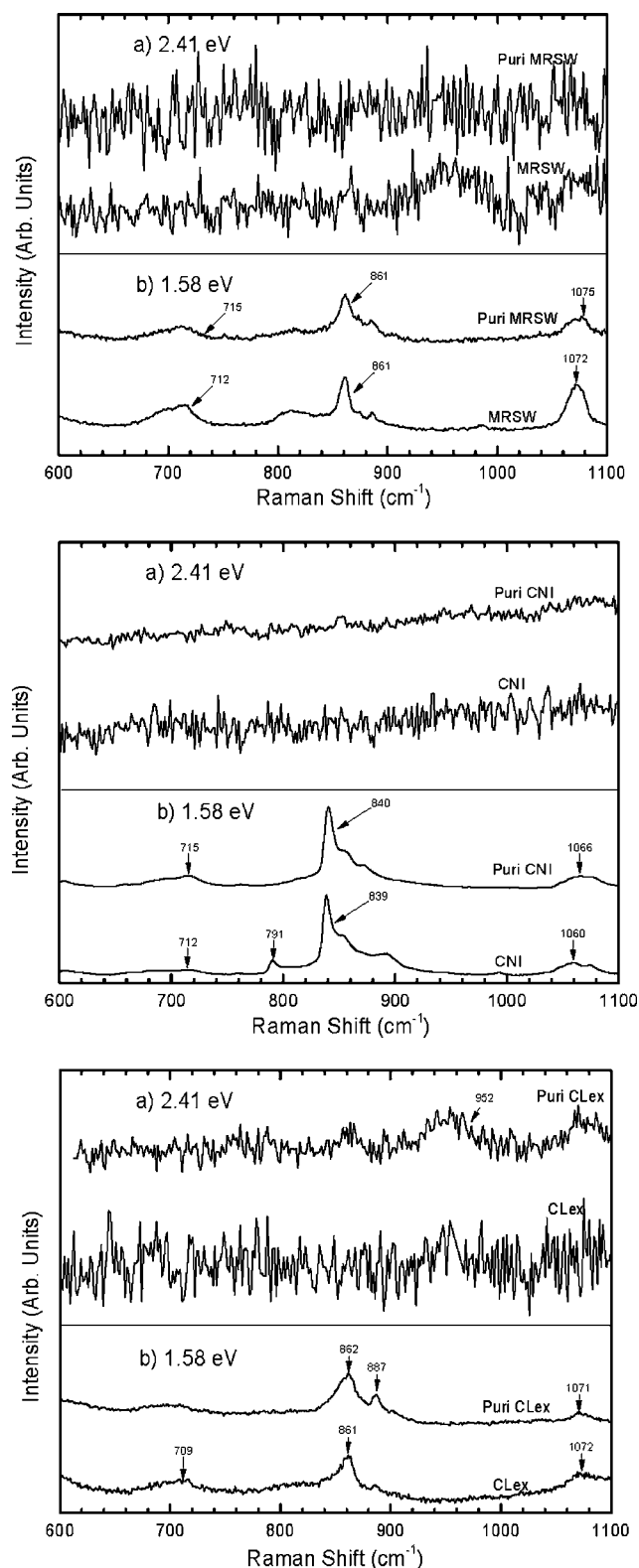


**Figure 3.** Comparison of Raman spectra after purification in the IFM range (600–1100  $\text{cm}^{-1}$ ). Each spectrum has been normalized toward the most intensive peak in the frequency range. (a) 2.41 eV and (b) 1.58 eV excitation energy.

this date, however, the origin of this IFM activation is not clearly understood. In this study, we focus on the effects of purification and synthesis methods on the IFM. These results are shown in Figure 3.

All three samples have Raman peaks in the IFM region at 1.58-eV excitation energy. Three discrete peaks can be identi-

fied: 710, 840/860, and 1070  $\text{cm}^{-1}$ . For MRSW and CLeX, synthesized by CAD, the Raman frequencies are very close. CNI differs from MRSW and CLeX in that it has a peak around 840  $\text{cm}^{-1}$ , while the other two have peaks around 860  $\text{cm}^{-1}$ . The purification does not change the spectra for any of the three samples, as the frequency and line shape before and after purification are comparable.

In contrast to the well-defined peaks excited at 1.58 eV, at 2.41-eV excitation, only a very weak peak for purified CLeX can be observed. This result differs from that of Alvarez et al.,<sup>46</sup> who showed distinguishable peaks at 2.41 eV for CAD-prepared SWNT bundles. Chen et al.<sup>47</sup> reported similar data. They observed the IFM only at 1064 nm (1.17-eV) excitation for HiPco samples and ascribed the appearance of the IFM to the increased cross-section of semiconducting tubes with diameters less than 1 nm. Our case, however, cannot confirm the hypothesis of Chen et al., or vice versa. Purification selectively removes metallic tubes and increases the content of semiconducting tubes, as demonstrated both in our CAD samples (MRSW) or in the HiPco sample (CNI). In addition, larger-diameter tubes tend to be enriched upon purification because of the high reactivity of small tubes. There are, however, no changes evident in the IFM. Further Raman spectra should be acquired at lower laser excitation energy (such as 1.17 eV) to compare the population of small-diameter semiconducting tubes in our samples. Very recently, it has been proposed that the IFMs are due to the combinational mode of zone-folded optic and acoustic branches of 2D graphite and that they can only be activated within low-chiral-angle tubes (i.e., zigzag) at certain excitation energies.<sup>48</sup> The absence of an IFM at 2.41 eV for our CAD samples (MRSW and CLeX) may be due to the low content of zigzag-like semiconducting tubes. For the HiPco sample (CNI), the high content of metallic tubes may mask the IFM mode and lead to its absence at 2.41-eV excitation.

#### IV. Pelletizing Process

MRSW was selected to study the pelletizing process, because it demonstrated a high-hydrogen-adsorption capacity.<sup>20</sup> The Raman spectra of pelletized and bulk MRSW samples at 1.58 eV are shown in Figure 4. The 1.58-eV level of excitation energy was selected, because all Raman-active features including the IFM can be observed. Panel (a) demonstrates the differences in the RBM. RBM frequencies increase from 308 to 319  $\text{cm}^{-1}$  along with a change in fwhm from 17 to 27  $\text{cm}^{-1}$ . Because the RBM is a symmetric  $A_{1g}$  mode, the changes in frequency and line width unambiguously indicate increased coupling between neighboring tubes,<sup>18</sup> implying a decrease in intertube distance.

A notable change in the G band is the increase in  $G^+$  line width and decrease in metallic  $G^-$  line width, with a negligible effect on their frequencies. Because the  $G^+$  band is due to vibrations along the tube axis, and the  $G^-$  band to vibrations along the circumference, the constant line position implies that no conformation change occurs during pelletization, which is in accordance with their high Young's modulus.<sup>49</sup> The increased  $G^+$  line width can be explained by the reduced distance between tubes in the pellet. Because the distance is smaller than the excitation wavelength can resolve, the line width is increased.<sup>50</sup> For metallic tubes represented by  $G^-$  values around 1545  $\text{cm}^{-1}$ , the decrease in line width may come from the fact that the increased coupling between neighboring metallic and semiconducting tubes reduces the coupling between tangential phonon modes and the electronic continuum spectrum in the inhomogeneous SWNT bundles.<sup>29</sup>

The most striking feature in the Raman spectra is the change in  $I_D/I_G$  ratio. After pelletization, the ratio increases from 0.034

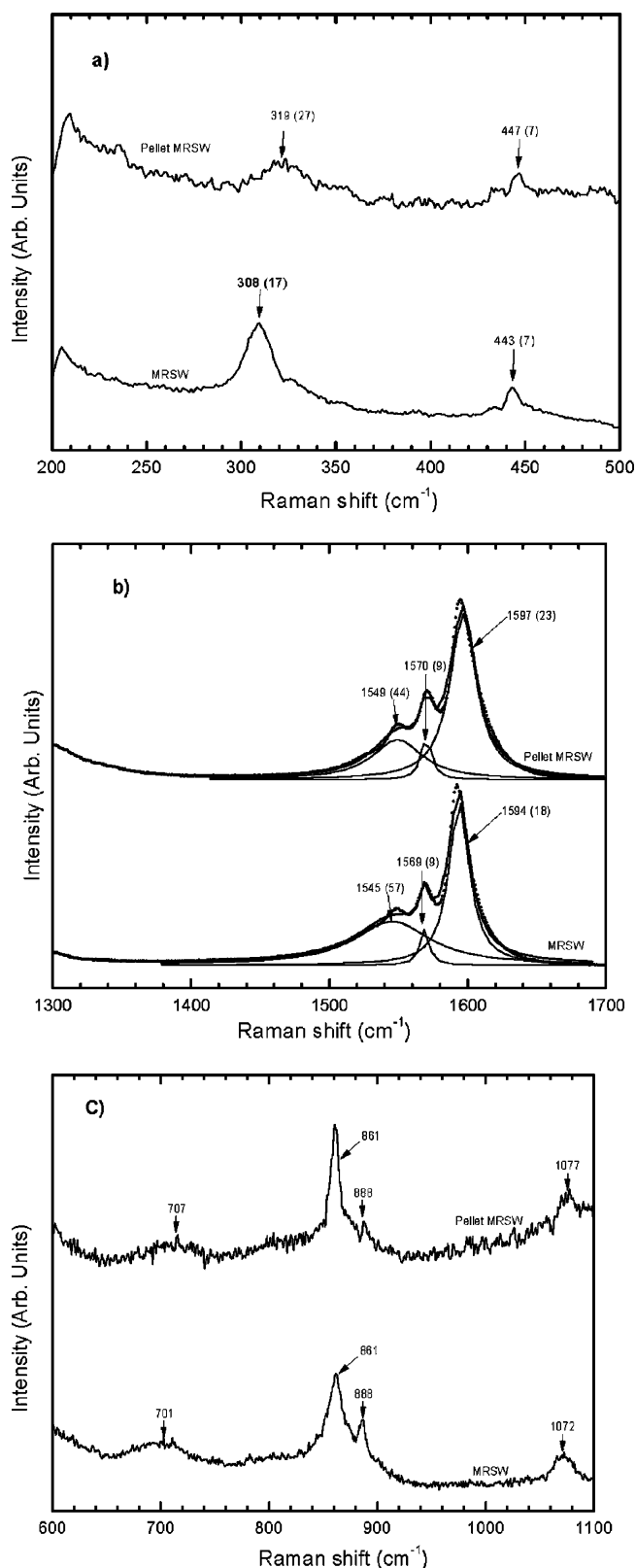


**Figure 4.** Raman spectra changes upon pelletization at a pressure of  $\sim 8.8$  MPa at excitation energy of 1.58 eV. Panel (a) RBM band, (b) G-band, (c) IFM, (d) post G-band mode (1700–2100  $\text{cm}^{-1}$ ). Dotted line, Raman spectra; thick solid line, summation of peak decomposition; thin solid line, deconvoluted G-band. Number in parentheses is the fwhm of the peak.

to 0.20, nearly sixfold. Because the constant G-band position excludes the possibility of tube bending, it may be related to the higher density of defects in the SWNT pellet due to the



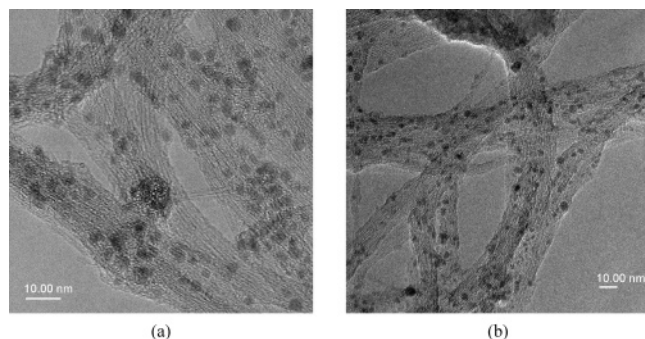


**Figure 5.** TEM micrograph of CNI samples dispersed with surfactant. (a) Pristine CNI; (b) dispersed CNI in 1 wt % SDS solution. Note the amorphous layer outside the bundles in (b).

increased tube density. In addition, the IFM does not change much, as shown in panel (c) of Figure 4. If the Raman-active mode originated from the symmetry-lowering effect due to the finite size of the tubes as proposed,<sup>45</sup> we should at least be able to observe significant changes in the IFM due to the increased coupling between tubes. However, the resonant electronic transition energy may change after pelletization because of stronger coupling between tubes, contributing to the unchanged IFM. More excitation lines (especially low-energy lines) should be used to observe the changes in IFM.

## V. Surfactant-Assisted Dispersion Process

Because of their popularity in characterization<sup>18,36</sup> and separation<sup>33</sup> studies, we chose CNI to investigate a surfactant-assisted dispersion process. As shown in Table 1, the average bundle sizes did not change significantly even under the harsh oxidative acid treatment for CNI. After sonication, the morphology of the CNI sample was analyzed and is summarized in Table 1. The average bundle size decreased significantly after sonication from 11.4 to 4.9 nm, and the maximum bundle size observed dwindled to ca. one-half that of the pristine sample. The sonication process effectively broke the relatively large bundle ( $\sim 12$  tubes/bundle) into smaller ones ( $\sim 5$ – $6$  tubes/bundle) or even individual tubes. The smaller bundles were inferred to be stabilized by surfactant SDS preventing further recombination after sonication. Figure 5 shows the morphology of the CNI sample dispersed in 1 wt % SDS solution. The amorphous layer outside the bundle is deduced to be SDS. We further confirmed the adsorption of SDS on SWNT bundles by electrophoresis. All CNI tubes moved to the cathode, which implies that the negatively charged SDS is attached around the CNI bundles.

Raman spectra at 1.58 eV of the CNI samples before and after sonication in SDS are shown in Figure 6. Once again, we focus on the spectrum acquired at 1.58-eV excitation, because all Raman features can be monitored at this excitation energy. It was shown previously that SDS had no effect on the Raman spectra.<sup>51</sup> Therefore, the change of the Raman features might be solely due to the dispersion effect. After sonication, the main bands such as the IFM and G band barely show any change. The main difference before and after dispersion is the disappearance of the peak at  $233\text{ cm}^{-1}$ , located in the RBM region. Larger tubes in the inhomogeneous tube bundle, such as that represented by the  $233\text{-cm}^{-1}$  peak, will lead to a size mismatch in the bundle, aiding the split into smaller bundle sizes according to the proposed dispersion mechanism.<sup>28,52</sup> It seems that the bundles with small tubes (CNI, 1.0 nm) are hard to break, even at 220 W of ultrasonication power. Another interesting feature in the Raman spectra is the nearly constant  $I_D/I_G$  ratio (sonicated sample, 0.052, vs pristine, 0.057). Although the bundles with

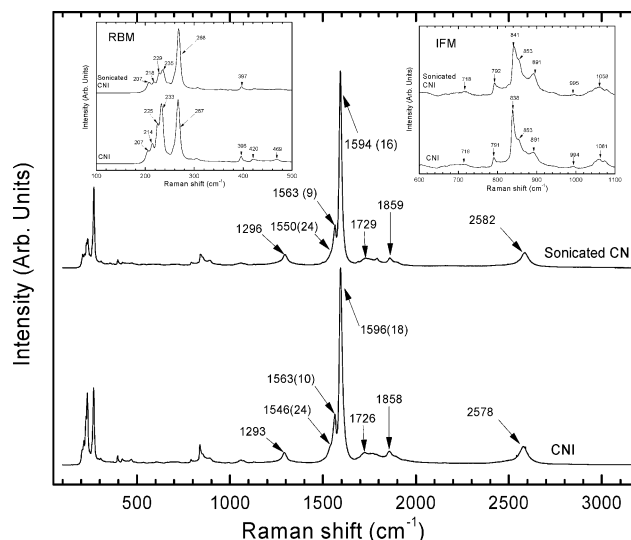


**Figure 6.** Raman spectra of CNI samples before and after dispersion in 1 wt % SDS at 1.58 eV excitation. Left inset: comparison of RBM before and after sonication. Right inset: IFM before and after sonication. Numbers in parentheses are the fwhm's of the corresponding peaks after deconvolution.

reduced size lead to changes in the resonant electronic transitions and thus are out of resonance at a fixed excitation wavelength,<sup>28</sup> the nearly constant  $I_D/I_G$  ratio suggests that the robust tube structure can maintain structural integrity despite the high shear forces in ultrasonication.

## VI. Conclusion

In this study, we combine TEM with RRS to study the effect of several processes relevant to composite and hydrogen storage applications, such as purification, pelletization, and debundling. The SWNT bundle size did not change significantly upon purification although smaller bundles were generated. RRS results reveal the preferred removal of metallic and small-diameter tubes due to their higher reactivity toward oxidative acid. The air-oxidation stage in the purification process removes most functional groups which were formed during the acid treatment. To obtain a high yield from purification, the air-oxidation step can be substituted by high-vacuum treatment.<sup>24</sup> Pelletizing under mild pressures ( $\sim 8.8$  MPa) reduces tube–tube distances. The  $I_D/I_G$  ratio is a sensitive indicator of packing of SWNTs. Finally, we show that SWNT bundles composed of large tubes tend to debundle during dispersion by ultrasonication in the presence of SDS. SWNTs synthesized with the HiPco process endure the high shear forces of ultrasonication without damage to the tube wall.

**Acknowledgment.** This material is based on work supported by the NSF under grant 0107710. K.S. thanks the Richard A. Matuszeski Research Fund for its support. S.C. would like to thank EPSCoR NSF grant 0132632 for funding this work. Some research was conducted at the Transmission Electron Microscopy Laboratory in the Department of Earth and Planetary Sciences of the University of New Mexico, which is partially supported by the NSF and State of New Mexico. S.R. thanks the NIH INBRE Award under grant 2P20RR016480-04.

## References and Notes

- Baughman, R. H.; Zakhidov, A. A.; de Heer, W. A. *Science* **2002**, 297, 787.
- Ajayan, P. M.; Ebbesen, T. W. *Rep. Prog. Phys.* **1997**, 60, 1025.



- (3) Ding, R. G.; Lu, G. Q.; Yan, Z. F.; Wilson, M. A. *J. Nanosci. Nanotechnol.* **2001**, *1*, 7.
- (4) Hirscher, M.; Becher, M. *J. Nanosci. Nanotechnol.* **2003**, *3*, 3.
- (5) Dresselhaus, M. S.; Avouris, P. Introduction to Carbon Material Research. In *Carbon Nanotubes*; Dresselhaus, M. S., Dresselhaus, G., Avouris, P., Eds.; Springer-Verlag Berlin: Berlin, 2001; Vol. 80, p 1.
- (6) Dresselhaus, M. S.; Eklund, P. C. *Adv. Phys.* **2000**, *49*, 705.
- (7) Ouyang, M.; Huang, J. L.; Lieber, C. M. *Acc. Chem. Res.* **2002**, *35*, 1018.
- (8) Rao, A. M.; Richter, E.; Bandow, S.; Chase, B.; Eklund, P. C.; Williams, K. A.; Fang, S.; Subbaswamy, K. R.; Menon, M.; Thess, A.; Smalley, R. E.; Dresselhaus, G.; Dresselhaus, M. S. *Science* **1997**, *275*, 187.
- (9) Dresselhaus, M. S.; Eklund, P. C. *Adv. Phys.* **2000**, *49*, 705.
- (10) Saito, R.; Kataura, H. Optical properties and Raman spectroscopy of carbon nanotubes. In *Carbon Nanotubes*; Dresselhaus, M. S., Dresselhaus, G., Avouris, P., Eds.; Springer-Verlag Berlin: Berlin, 2001; Vol. 80, p 213.
- (11) Dresselhaus, M. S.; Rao, A. M.; Dresselhaus, G. *Encycl. Nanosci. Nanotechnol.* **2004**, *9*, 307.
- (12) Ebbesen, T. W. Production and purification of carbon nanotubes. In *Carbon Nanotubes*; Ebbesen, T. W., Ed.; CRC: Boca Raton, 1997; p 139.
- (13) Dillon, A. C.; Gennett, T.; Jones, K. M.; Alleman, J. L.; Parilla, P. A.; Heben, M. J. A simple and complete purification of single-walled carbon nanotube materials. *Adv. Mater.* **1999**, *11* (16), 1354–1358.
- (14) Dresselhaus, M. S.; Williams, K. A.; Eklund, P. C. *MRS Bull.* **1999**, *45*.
- (15) Williams, K. A.; Eklund, P. C. *Chem. Phys. Lett.* **2000**, *320*, 352.
- (16) Yin, Y. F.; Mays, T.; McEnaney, B. *Langmuir* **2000**, *16*, 10521.
- (17) Shen, K.; Pietrass, T. *Appl. Phys. Lett.* **2004**, *84*, 1567.
- (18) O'Connell, M. J.; Bachilo, S. M.; Huffman, C. B.; Moore, V. C.; Strano, M. S.; Haroz, E. H.; Rialon, K. L.; Boul, P. J.; Noon, W. H.; Kittrell, C.; Ma, J.; Hauge, R. H.; Weisman, R. B.; Smalley, R. E. *Science* **2002**, *297*, 593.
- (19) Niyogi, S.; Hamon, M. A.; Hu, H.; Zhao, B.; Bhowmik, P.; Sen, R.; Itkis, M. E.; Haddon, R. C. *Acc. Chem. Res.* **2002**, *35*, 1105.
- (20) Shen, K.; Xu, H.; Jiang, Y.; Pietrass, T. *Carbon* **2004**, *42*, 2315.
- (21) Hirscher, M.; Becher, M.; Haluska, M.; Dettlaff-Weglikowska, U.; Quintel, A.; Duesberg, G. S.; Choi, Y. M.; Downes, P.; Hulman, M.; Roth, S.; Stepanek, I.; Bernier, P. *Appl. Phys. A* **2001**, *72*, 129.
- (22) Li, Y.; Mann, D.; Rolandi, M.; Kim, W.; Ural, A.; Hung, S.; Javey, A.; Cao, J.; Wang, D.; Yenilmez, E.; Wang, Q.; Gibbons, J. F.; Nishi, Y.; Dai, H. *Nano Lett.* **2004**, *4*, 317.
- (23) Maarouf, A. A.; Kane, C. L.; Mele, E. J. *Phys. Rev. B* **2000**, *61*, 11156.
- (24) Kuznetsova, A.; Yates, J. T.; Liu, J.; Smalley, R. E. *J. Chem. Phys.* **2000**, *112*, 9590.
- (25) Ebbesen, T. W. *Annu. Rev. Mater. Sci.* **1994**, *24*, 235.
- (26) Dai, H. Nanotube Growth and Characterization. In *Carbon Nanotubes*; Dresselhaus, M. S., Dresselhaus, G., Avouris, P., Eds.; Springer-Verlag Berlin: Berlin, 2001; Vol. 80, p 29.
- (27) Nikolaev, P. *J. Nanosci. Nanotechnol.* **2004**, *4*, 307.
- (28) O'Connell, M. J.; Sivaram, S.; Doorn, S. K. *Phys. Rev. B* **2004**, *69*, 235415/1.
- (29) Brown, S. D. M.; Jorio, A.; Corio, P.; Dresselhaus, M. S.; Dresselhaus, G.; Saito, R.; Kneipp, K. *Phys. Rev. B* **2001**, *63*, 155414/1.
- (30) Dresselhaus, M. S.; Dresselhaus, G.; Jorio, A.; Souza Filho, A. G.; Saito, R. *Carbon* **2002**, *40*, 2043.
- (31) Jorio, A.; Saito, R.; Hafner, J. H.; Lieber, C. M.; Souza Filho, A. G.; Pimenta, M. A.; Matinaga, F. M.; Dantas, M. S. S.; Hunter, M.; McClure, T.; Dresselhaus, G.; Dresselhaus, M. S. *AIP Conf. Proc.* **2001**, *591*, 298.
- (32) Kataura, H.; Kumazawa, Y.; Maniwa, Y.; Umez, I.; Suzuki, S.; Ohtsuka, Y.; Achiba, Y. *Synth. Met.* **1999**, *103*, 2555.
- (33) Strano, M. S.; Dyke, C. A.; Usrey, M. L.; Barone, P. W.; Allen, M. J.; Shan, H.; Kittrell, C.; Hauge, R. H.; Tour, J. M.; Smalley, R. E. *Science* **2003**, *301*, 1519.
- (34) Dresselhaus, M. S.; Dresselhaus, G.; Jorio, A.; Souza Filho, A. G.; Samsonidze, G. G.; Saito, R. *J. Nanosci. Nanotechnol.* **2003**, *3*, 19.
- (35) Jorio, A.; Saito, R.; Hafner, J. H.; Lieber, C. M.; Hunter, M.; McClure, T.; Dresselhaus, G.; Dresselhaus, M. S. *Phys. Rev. Lett.* **2001**, *86*, 1118.
- (36) Bachilo, S. M.; Strano, M. S.; Kittrell, C.; Hauge, R. H.; Smalley, R. E.; Weisman, R. B. *Science* **2002**, *298*, 2361.
- (37) Milner, M.; Kurti, J.; Hulman, M.; Kuzmany, H. *Phys. Rev. Lett.* **2000**, *84*, 1324.
- (38) Kurti, J.; Zolyomi, V.; Kertesz, M.; Sun, G.; Baughman, R. H.; Kuzmany, H. *Carbon* **2004**, *42*, 971.
- (39) Jorio, A.; Fantini, C.; Dantas, M. S. S.; Pimenta, M. A.; Souza Filho, A. G.; Samsonidze, G. G.; Brar, V. W.; Dresselhaus, G.; Dresselhaus, M. S.; Swan, A. K.; Unlu, M. S.; Goldberg, B. B.; Saito, R. *Phys. Rev. B* **2002**, *66*, 115411/1.
- (40) Kurti, J.; Zolyomi, V.; Gruneis, A.; Kuzmany, H. *Phys. Rev. B* **2002**, *65*, 165433/1.
- (41) Brown, S. D. M.; Jorio, A.; Dresselhaus, M. S.; Dresselhaus, G. *Phys. Rev. B* **2001**, *64*, 073403/1.
- (42) Thomsen, C.; Reich, S. *Phys. Rev. Lett.* **2000**, *85*, 5214.
- (43) Ferrari, A. C.; Robertson, J. *Phys. Rev. B* **2000**, *61*, 14095/1.
- (44) Saito, R.; Takeya, T.; Kimura, T.; Dresselhaus, G.; Dresselhaus, M. S. *Phys. Rev. B* **1998**, *57*, 4145.
- (45) Saito, R.; Takeya, T.; Kimura, T.; Dresselhaus, G.; Dresselhaus, M. S. *Phys. Rev. B* **1999**, *59*, 2388.
- (46) Alvarez, L.; Righi, A.; Guillard, T.; Rols, S.; Anglaret, E.; Laplace, D.; Sauvajol, J. L. *Chem. Phys. Lett.* **2000**, *316*, 186.
- (47) Chen, G.; Sumanasekera, G. U.; Pradhan, B. K.; Gupta, R.; Eklund, P. C.; Bronikowski, M. J.; Smalley, R. E. *J. Nanosci. Nanotechnol.* **2002**, *2*, 621.
- (48) Fantini, C.; Jorio, A.; Souza, M.; Ladeira, L. O.; Souza Filho, A. G.; Saito, R.; Samsonidze, G. G.; Dresselhaus, G.; Dresselhaus, G.; Pimenta, M. A. *Phys. Rev. Lett.* **2004**, *93*, 087401.
- (49) Treacy, M. M. J.; Ebbesen, T. W.; Gibson, J. M. *Nature* **1996**, *381*, 678.
- (50) Jorio, A.; Souza Filho, A. G.; Dresselhaus, G.; Dresselhaus, M. S.; Swan, A. K.; Unlu, M. S.; Goldberg, B. B.; Pimenta, M. A.; Hafner, J. H.; Lieber, C. M.; Saito, R. *Phys. Rev. B* **2002**, *65*, 155412/1.
- (51) Moore, V. C.; Strano, M. S.; Haroz, E. H.; Hauge, R. H.; Smalley, R. E.; Schmidt, J.; Talmon, Y. *Nano Lett.* **2003**, *3*, 1379.
- (52) Strano, M. S.; Moore, V. C.; Miller, M. K.; Allen, M. J.; Haroz, E. H.; Kittrell, C.; Hauge, R. H.; Smalley, R. E. *J. Nanosci. Nanotechnol.* **2003**, *3*, 81.